PLANETARY SCIENCE

Searching for surficial water ice in lunar permanently shaded regions (PSRs) with ShadowCam

Shuai Li[1]*, Mark S. Robinson[2], Brett W. Denevi[3], Madeleine R. Manheim[2], Erwan Mazarico[4], Robert V. Wagner[2], Emerson J. Speyerer[2], Prasun Mahanti[2]

Airless bodies such as the Moon, Mercury, and Ceres have permanently shaded regions (PSRs) that can cold trap water ice. Mercury and Ceres have substantial ice deposits in their PSRs, but lunar water ice distribution remains uncertain because of sparse detections and limited data. Here, we assessed surficial water ice in lunar PSRs using high-resolution observations from ShadowCam onboard the Korea Pathfinder Lunar Orbiter. We used the high-reflectance and forward-scattering optical properties to search for water ice in lunar PSRs. We found no evidence of widespread water ice in PSRs at abundances above the detection limit of 20 to 30 wt % but could not rule out widespread low-content water ice. A few small locations with both high reflectance and forward-scattering behavior were observed, which could be consistent with >10 wt % ice. Future missions with low detection limits (<1 wt %) of water ice can test our findings.

INTRODUCTION

Airless planetary bodies with minimal axial tilt, such as the Moon, Mercury, and Ceres, have permanently shaded regions (PSRs) near their respective poles where direct sunlight never reaches (*1*). These PSRs create ultracold environments where temperatures remain exceedingly low over geological timescales, which could permit volatiles like water ice to accumulate and persist (*2*–*4*). Understanding the accumulation and preservation of water ice in PSRs on those planetary bodies is fundamental to unraveling volatile origins in the inner Solar System, particularly the origin of water on Earth.

Observations of Mercury and Ceres have confirmed the prediction concerning cold trapping of water in PSRs by revealing substantial ice deposits within their extremely cold PSRs (≲110 K). On Mercury, ground-based radar and the MESSENGER (Mercury Surface, Space Environment, Geochemistry, and Ranging) observations revealed thick (tens of meters), nearly pure ice deposits in polar craters, showing that cold PSRs can effectively trap water ice (*5*–*11*). Similarly, the Dawn spacecraft detected bright deposits of surface water ice and strong neutron suppression of subsurface ice in Ceres's PSRs, indicating substantial water inventories, although the ice is not as pure as that on Mercury (*12*–*14*). The difference in ice purity on Ceres and Mercury may be due to the shorter lifetimes of Ceres's PSRs caused by higher obliquity and orbital dynamics, leading to less efficient preservation of ice (*15*, *16*).

In contrast, the Moon presents a puzzling case. Despite its PSRs being old (*17*, *18*) and cold enough to support ice accumulation (*2*, *3*, *19*), the radar, neutron, and visible image observations have not definitively detected ice deposits (*20*–*27*). However, several missions have provided indirect evidence of surface water ice on the Moon. The LCROSS impact mission detected water vapor and other volatiles upon impacting the Cabeus PSR, suggesting the presence of subsurface and/or surface ice (*28*). The Lunar Orbiter Laser Altimeter (LOLA) aboard the Lunar Reconnaissance Orbiter (LRO) observed increased surface albedo in some PSRs, consistent with surface frost or immature regolith (*29*, *30*). The Chandrayaan-1 CHACE instrument also detected water molecules in the lunar exosphere from mid-latitudes to the poles, consistent with a surface or subsurface water source (*31*). Frequent water plumes were recently suggested to be present near the lunar poles at nighttime by Kaguya SP (Spectral Profiler) data, which might be sourced from subsurface and/or surface water ice (*32*). Although instruments such as the Lyman-Alpha Mapping Project (LAMP) onboard LRO and the Moon Mineralogy Mapper (M^3) onboard Chandrayaan-1 have detected surficial water ice in lunar PSRs, the ice appears patchy and of low abundance (*33*–*35*). It is noteworthy that the ice detections by LAMP and M^3 are limited by the data quality [e.g., low signal-to-noise ratios (SNRs)] (*33*, *34*). It is unclear whether LAMP and M^3 could only detect regions with high ice concentrations and showed no detections when ice content is low but widespread, which resulted in the biased impression of patchiness. Nevertheless, it raises questions about whether the lunar PSRs accumulate water ice as extensively as previously anticipated (*2*, *3*).

To understand the disparity of surficial water ice between the Moon and other bodies like Mercury, previous studies investigated potential factors that could affect ice accumulation and preservation. Slight differences in volatile delivery, such as water-rich impacts and solar wind contributions, are insufficient to account for the disparity in ice content between the Moon and Mercury. The impact flux of water-rich comets and carbonaceous chondrites on Mercury is estimated to be a few times to around 20 times higher than that on the Moon (see Methods) [e.g., (*36*)]. However, the higher impact velocity on Mercury is suggested to generate 20 times more vapor and, thus, more water loss than those on the Moon (*37*). Thus, the impact delivery of water to Mercury and the Moon may be similar (see Methods). Although it is suggested that solar wind may induce 10s to ~100 times more H_2O on the Mercury surface than the lunar surface because of the much higher temperatures of the former (*38*, *39*), H_2O has much shorter lifetime and, thus, much less chance to migrate to cold traps on Mercury than the Moon [e.g., (*40*)]. Unlike Mercury and the Moon, Ceres PSRs receive extensive water supplies from subsurface sources that vary seasonally (*41*), which explains the widespread water ice deposits observed in these regions (*12*, *14*). In contrast, the PSRs on the Moon and Mercury lack comparable supplies.

[1]Hawaii Institute of Geophysics and Planetology, University of Hawaii at Manoa, Honolulu, HI, USA. [2]Intuitive Machines, Phoenix, AZ, USA. [3]Johns Hopkins University Applied Physics Laboratory, Laurel, MD, USA. [4]NASA Goddard Space Flight Center, Greenbelt, MD, USA.
*Corresponding author. Email: shuaili@hawaii.edu

Destruction processes may influence the distribution and abundance of lunar ice. The lack of a global magnetic field on the Moon exposes its surface directly to solar wind sputtering and ultraviolet and cosmic radiations, which can erode surface ice over time [e.g., (*42*)]. However, similar sputtering and radiation destruction processes also operate on Mercury where its tenuous magnetic field cannot completely block the solar wind. Studies suggest that the flux of solar wind reaching Mercury is comparable to that on the Moon (*43*). Alternatively, enhanced bombardment by larger meteoroids (1 cm to 100 m in size range) on the Moon may have intensified impact gardening, which may disrupt surface ice and increase sublimation rates (*44*–*46*). However, the higher impact velocity on Mercury was suggested to generate 20 times more vapor than on the Moon (*37*), which may cause the higher water loss of the former. Thus, impact destruction of water ice on Mercury and the Moon may not be substantially different. Other minor factors such as vertical migration of water molecules driven by thermal pumping operate similarly in PSRs on the Moon, Mercury, and possibly other airless bodies, and they contribute limited effects on the distribution and abundance of water ice (*47*).

Given that the Moon may receive comparable or slightly less water supplies and similar destruction processes compared to Mercury, it is expected to see widespread but lower ice contents in lunar PSRs than Mercury's (*3*). However, the sparse ice detections in lunar PSRs suggest that the current hypothesis concerning water cold trapping (*2*, *3*) needs to be refined; otherwise, those ice detections should be challenged. All previous data cannot resolve whether the observed patchiness of lunar water ice, such as by LAMP and M^3, is a true representation of its distribution or an artifact resulting from limitations in low SNRs of data and coverage. Higher spatial resolution and SNR data than current datasets such as LAMP and M^3 are essential to determine whether the lunar PSRs accumulate water ice as extensively as current hypotheses predict. The visible wavelength images recently acquired by ShadowCam, onboard the Korea Pathfinder Lunar Orbiter (KPLO), with its <2-m pixel scale and high SNR (50 to 100 in most PSRs), provide an unprecedented opportunity to perform such assessments. We present results of searching for surficial water ice in lunar PSRs with ShadowCam observations to advance our understanding of cold trapping processes of water on the Moon.

Overview of method

We examined two diagnostic optical properties of water ice to search for its surficial distribution in lunar PSRs. Water ice is known for notably higher visible reflectance (*9*) and stronger forward scattering than typical lunar regolith (Fig. 1, A and B) (*48*, *49*). Orbital observations demonstrated that water ice deposits in PSRs on Mercury and Ceres exhibit around two times higher reflectance than their surroundings in visible-wavelength images (*9*, *10*, *12*, *14*). However, similar detections on the Moon remain elusive (*25*, *27*) because of limitations in previous datasets (*50*). We conducted laboratory experiments and radiative transfer models to determine the detection

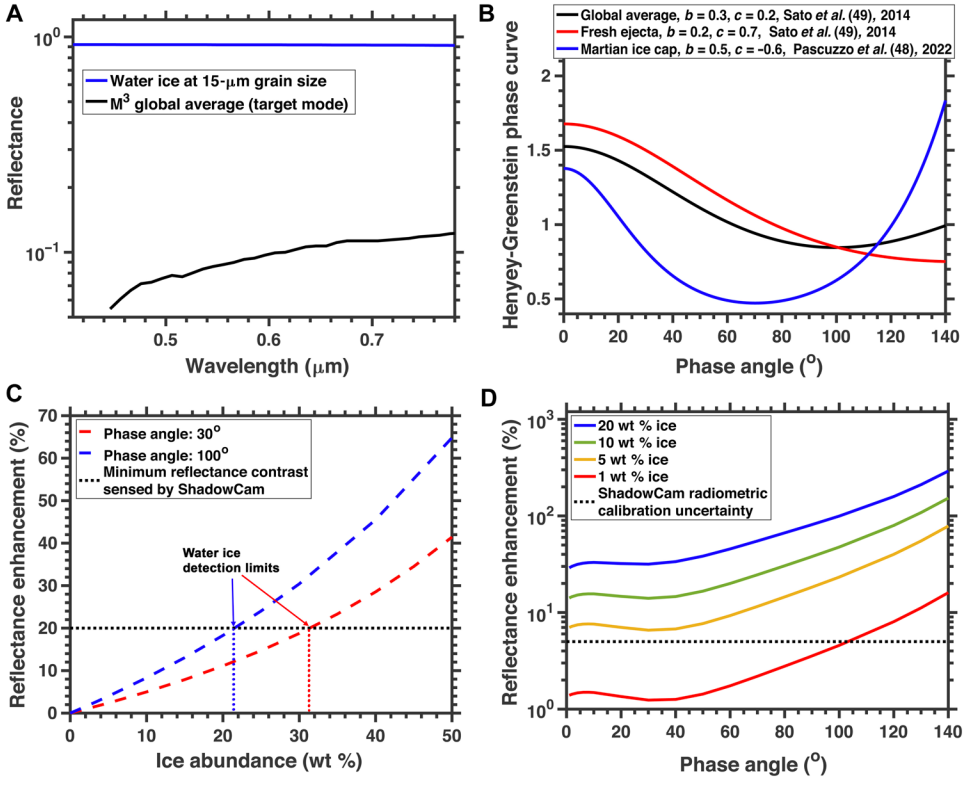

Fig. 1. Reflectance and scattering properties of water ice and lunar regolith. (**A**) Reflectance spectra (410 to 780 nm) of pure ice derived from (*76*) and global lunar surface derived from M^3 (*34*). (**B**) Phase curves of the global lunar surface, fresh ejecta on the Moon, and the Martian ice cap (*48*, *49*). (**C**) Modeled reflectance enhancement at 700 nm as a function of ice content at two phase angles (see Methods). The minimum reflectance contrast sensed by ShadowCam is from (*54*). (**D**) Modeled reflectance enhancement as a function of phase angle for multiple ice contents.

limits for using the two optical properties of water ice. Our findings indicated that the detection limit with visible reflectance enhancement is ~20 to 30 wt % ice, which varies with phase angle (Fig. 1C). The detection limit of water ice decreases from around 30 wt % at a 30° phase angle to around 20 wt % at a 100° phase angle (Fig. 1C). This is in general agreement with previous laboratory experiments (*51*, *52*), although the laboratory experiment using mare regolith simulant suggested a slightly higher detection limit at around 35 wt % (*52*).

Our radiative transfer modeling results suggest that the ice-regolith mixtures become more forward scattering with increasing ice content. We find that forward-scattering analysis offers a more sensitive detection capability, with a detection limit of around 5 wt % water ice (Fig. 1D) resulting from the accurate absolute radiometric calibration of ShadowCam data (5% uncertainty) (see Methods) (*53*). However, the detection limit of water ice based on its forward-scattering nature is around 20 to 30 wt % in previous laboratory experiments (*51*, *52*). The simulants used in those experiments show slightly forward scattering (*51*, *52*) rather than backscattering as real lunar regolith (*49*), which resulted in reduced scattering contrast and, thus, elevated detection limit of water ice. The two approaches enable an accurate evaluation of the surface ice distribution in lunar PSRs.

RESULTS

We found that the reflectance of boulders, bedrock, fresh craters, and ejecta can be around 10% to more than 100% higher (i.e., higher radiance values) than the surrounding regolith in ShadowCam data in lunar PSRs. Figure 2 shows examples seen in PSRs near the south and north poles, and their location information is listed in table S1 (see Methods for details of data preparation). The increased brightness is likely due to their relatively less weathered surfaces or because they are tilted toward the reflected light sources, resulting in lower incidence angles and, thus, higher radiance. To verify that these brightness patterns are not unique to polar regions, we examined ShadowCam images of temporarily shaded regions at low latitudes where ice is not stable. We observed similar brightness variations in these regions. For instance, the Sundman V crater located near 11.9°N and 93.6°W was imaged by ShadowCam and LROC NAC when it was in temporary shadow (Fig. 3A) and sunlit (Fig. 3B), respectively. We observed that rocks, boulders, fresh craters, and ejecta are much brighter than their surrounding regolith in both the ShadowCam and NAC images (Fig. 3). Similar cases were seen in many other ShadowCam and NAC images taken at PSR analogs in temporary shadow and sunlight, respectively (e.g., Aristarchus crater in fig. S1) (*54*). Together, it confirms that such bright patterns are not necessarily indicative of ice.

Regions that are brighter than their surroundings but lack identifiable boulders, fresh impact craters, or any other recent exposures such as landslides are intriguing. We define these regions as high-reflectance anomalies. These areas are candidates for the presence of surface ice. We identified several small areas in PSRs with elevated reflectance that are not associated with resolved boulders, fresh

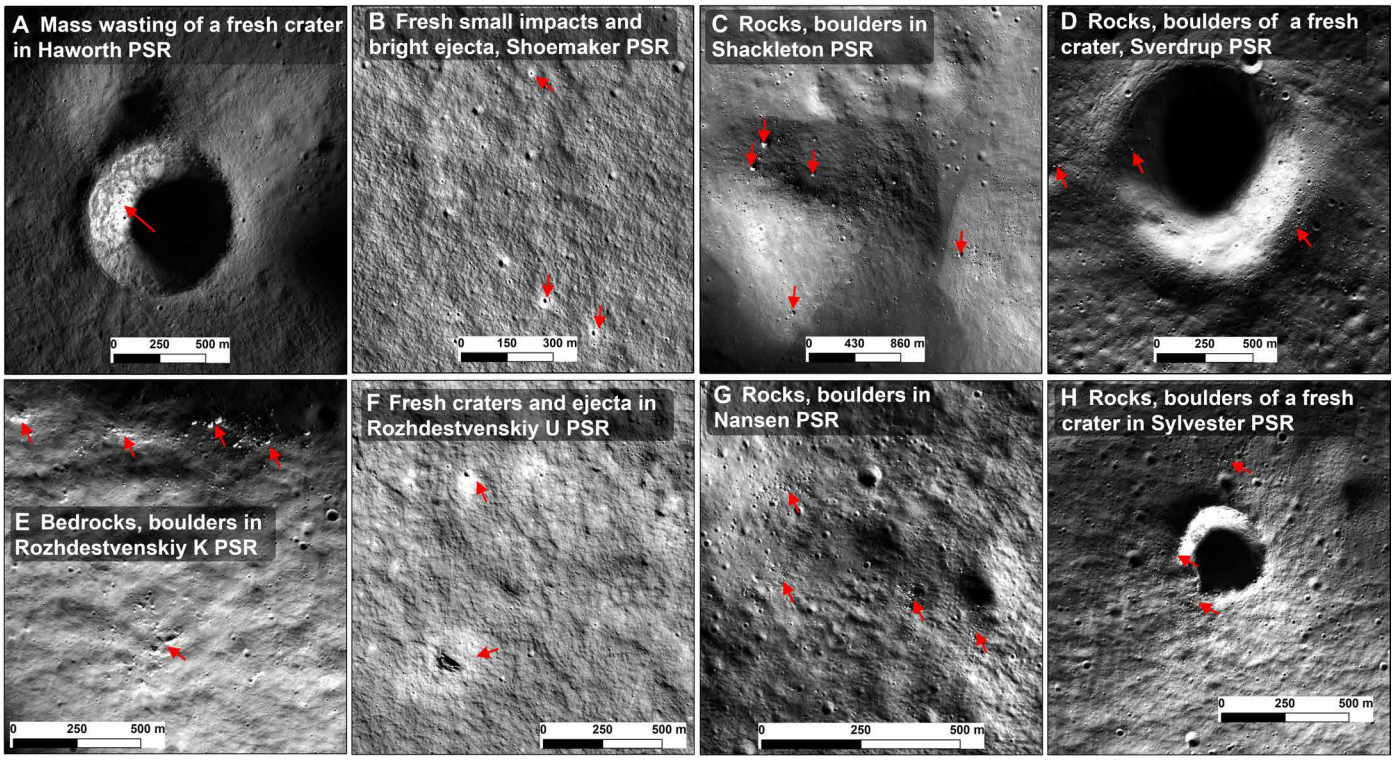

Fig. 2. Examples of bright exposures (pointed by red arrows) commonly seen in lunar PSRs. (**A**) Recent mass wasting on a small crater wall inside Haworth PSR. (**B**) A few small fresh craters and their bright ejecta inside the Shoemaker PSR. (**C**) Bright boulders seen on the Shackleton PSR crater floor. (**D**) Exposures of bright boulders in and out of a small crater inside the Sverdrup PSR. (**E**) Bright bedrocks and boulders seen in the Rozhdestvenskiy K PSR. (**F**) Fresh craters and their bright ejecta in the Rozhdestvenskiy U PSR. (**G**) Bright rocks and boulders seen in the Nansen PSR. (**H**) Bright rocks and boulders near a fresh crater in the Sylvester PSR. These examples were from regional mosaics of ShadowCam images (see Methods), and individual ShadowCam image IDs were not tracked.

craters, ejecta, or other fresh exposures (Fig. 4 and fig. S2). Figure 4 shows one of these examples within the de Gerlache PSR. There is no resolvable shadow near the bright spot under multiple lighting conditions, recognizing that they do not change much. It is noteworthy that craters smaller than the bright spot shown in Fig. 4 can be well resolved by ShadowCam images (fig. S3), which rules out the possibility of the bright spot being a fresh crater. The size and location of the bright spot exhibit no measurable change under various illumination conditions, which suggests that the elevated reflectance at this spot is not introduced by local topography and reflects the intrinsic albedo of the surface material. ShadowCam images indicate that the bright spot in Fig. 4 has 50 to 60% higher reflectance than the immediate surroundings. Possible candidate materials are freshly exposed regolith (e.g., anorthosite) and water ice, both of which are known to have higher reflectance than the surface mature regolith on the Moon (Fig. 1) [e.g., (*55*)]. Thus, bright spots similar to that in Fig. 4 are candidates for surficial water ice or other types of volatile ice and materials with high reflectance in the visible region. However, we found that the vast majority of lunar PSRs showed no significant reflectance variations other than those associated with bedrock, boulders, fresh craters, or recent exposures like landslides (Fig. 2, A to H). This suggests that most lunar PSRs either lack surface ice or contain ice at concentrations below the detection limit of ShadowCam (20 to 30 wt % ice, Fig. 1C).

We analyzed ShadowCam stereo observations acquired at different phase angles to search for regions exhibiting forward-scattering anomalies (see Methods). We found that the ratio of ShadowCam-measured radiances between the lower phase (LP) and higher phase (HP) angles in each pair of stereo observations was typically greater than one, suggesting a decrease in reflectance as phase angles increases because of backward-scattering behavior (fig. S4). Bedrock, boulders, fresh craters and ejecta, and other fresh exposures exhibited even higher ratios than mature regolith, which is consistent with the backward-scattering nature of the lunar surface observed by the LROC WAC and NAC (*49*, *56*, *57*). On the floor of Hermite A crater within the PSR (Fig. 5, A and B), we observed that fresh craters and ejecta, boulders, bedrock, and recent mass wasting all exhibited high ratio values (>1). We observed similar scattering patterns in temporarily shadowed areas near the equator where ice is unstable. In Fig. 5 (C to E), we show a small area in Sundman V crater where ShadowCam stereo images were acquired while it was in temporary shadow. We then also examined a pair of overlapping NAC images obtained at two different phase angles when the crater was illuminated by the Sun, which resemble the illumination in the ShadowCam stereo observations. The fresh craters, ejecta, and boulders in this area exhibited much higher values than the surrounding background regolith when ratioing LP/HP angle ShadowCam images, and similar trends were seen in the similarly ratioed NAC images (Fig. 5, D and E). The paired observations of ShadowCam and LROC indicated that the backward-scattering behavior of the background regolith is common across the lunar surface and fresh exposures such as craters and ejecta, bedrock, boulders, and landslides are even more strongly backward scattering than the regolith (*49*, *54*, *56*–*58*). Such materials would provide a strong background contrast with water ice, which exhibits strong forward scattering.

We identified areas within PSRs that exhibit relatively strong forward scattering (e.g., Hapke's phase function parameter $c < 0$) within ShadowCam stereo images. We identified an example of the forward-scattering anomaly nearby a small crater (49.7281°W, 84.8041°S) within the Cabeus PSR (Fig. 6). Regions of interest (ROIs) 1, 2, and 3 in Fig. 6B are two or three times brighter than the immediate surroundings. However, ROI 1 showed much lower values (~0.8) in the ratio map (Fig. 6C) that we derived by dividing ShadowCam images acquired at an LP angle by those acquired at an HP

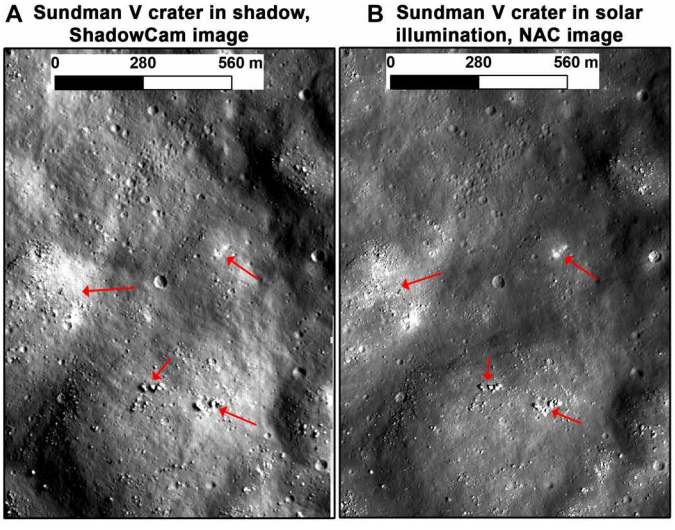

Fig. 3. Boulders, fresh craters and ejecta, and recent mass wasting (pointed by red arrows) are notably brighter than their surroundings. ShadowCam (M040154858SE) and NAC (M1106524331) images at Sundman V crater (11.960°N, 266.441°E) when it was in temporal shadow (**A**) and direct solar illumination (**B**), respectively.

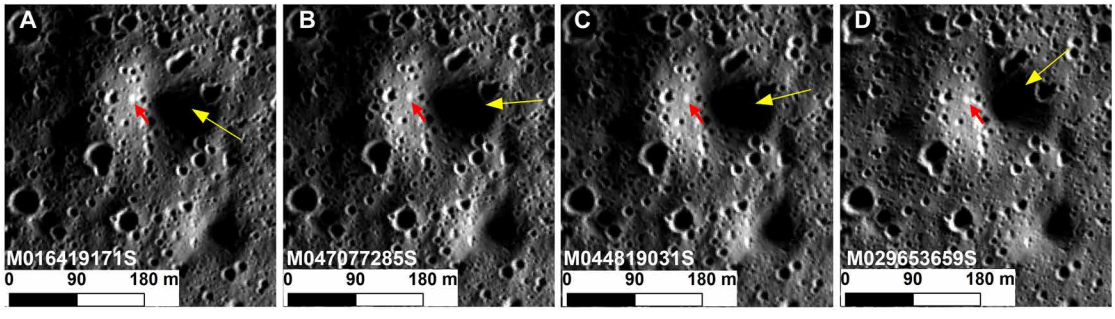

Fig. 4. Possible high-reflectance anomaly seen at de Gerlache PSR. (**A** to **D**) Same bright spot (red arrows) (88.5352°S, 97.4007°W) imaged by ShadowCam under different scattered light conditions. Yellow arrows approximately mark the dominant light sources in each image.

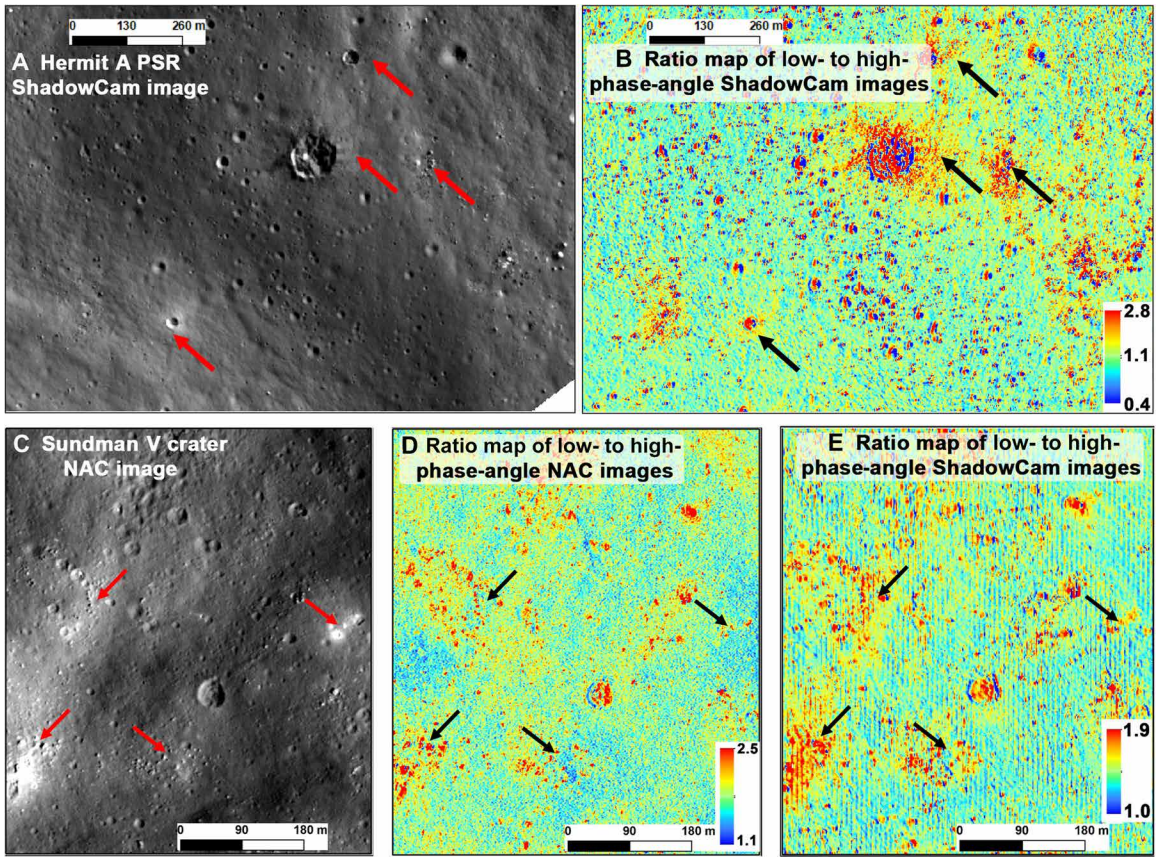

Fig. 5. Bedrock, boulders, fresh crater and ejecta, and recent mass wasting (red and black arrows) exhibit stronger backward scattering than their surroundings. (**A**) ShadowCam observation at Hermite A PSR (M029268387SE). (**B**) Ratio map of low- to high-phase-angle observations. (**C**) NAC images (M1106524331) at Sundman V crater near the equator. (**D** and **E**) Ratio maps of low- to high-phase-angle observations of NAC (under solar illumination) and ShadowCam (in shadow), respectively. Note that shaded regions (low data quality) were not masked in radiance ratios.

angle (LP/HP). This observation implied that reflectance increases at HP angles, consistent with a forward-scattering behavior (fig. S4). In contrast, the reference bright spots 2 and 3 (ROIs 2 and 3) and the surrounding background show values greater than 1 (~1.1 to 1.2) in the phase ratio map (Fig. 6C), indicating a decrease in reflectance with increasing phase angles and a backward-scattering behavior. To assess whether the observed differences in ratio values at spots 1 to 3 resulted from local topography, we examined a surface slope map (6 m/pixel) derived from ShadowCam stereo data. We found no abrupt slope changes at these spots compared with their immediate surroundings, with most variations being less than 2° (Fig. 6D), which indicated that the observed radiance and ratio variations could not be attributed to local topographic effects. It is noteworthy that slope changes at spots 1 and 2 (~5 by 5 pixels in the slope map) may not be well resolved in the slope map, which normally requires ~10 pixels or a larger size. The forward-scattering anomaly at spot 1 may be indicative of water ice bearing. The annual maximum temperature derived from Diviner at spot 1 (2 Diviner pixels) is around 92 K (*59*), which is low enough to preserve water ice over geological timescales (*4*). We performed forward Hapke radiative transfer modeling of lunar regolith and water ice (see Methods). The results showed that mixing a few wt % of ice into regolith can increase both the brightness and the forward-scattering properties of the mixture (fig. S4). To further assess the scattering properties in this region, we modeled the radiance ratios of typical lunar regolith, fresh highland impact ejecta, and water ice using Hapke's radiative transfer model under the ShadowCam viewing angles (see Methods). Our modeling results suggested that ROIs 2 and 3 mimic the backscattering behavior of fresh highland impact ejecta, while ROI 1 exhibits similar forward scattering to water ice (Fig. 7). The incidence, emittance, and phase angles were derived from ray tracing models under the ShadowCam image observation conditions (see Methods). Similar forward-scattering anomalies were also seen in Hermite A and Faustini PSRs (figs. S2 and S7). However, we only examined six pairs of ShadowCam stereo observations in this work. They were located at Faustini, Slater, Cabeus, and Wiechert J PSRs near the south pole, Hermite A and Mouchez L PSRs near the north pole. We expect to see more similar forward-scattering anomalies when ShadowCam will obtain more stereo observations during the KPLO extended mission.

DISCUSSION

Scattering properties of the lunar surface inferred from the ShadowCam stereo observations are helpful to discriminate dry boulders from ice-bearing ones. It is known that dry lunar boulders exhibit backward scattering (*49*, *56*), while mixing a small amount of ice can make them more forward scattering and brighter (fig. S4). In many

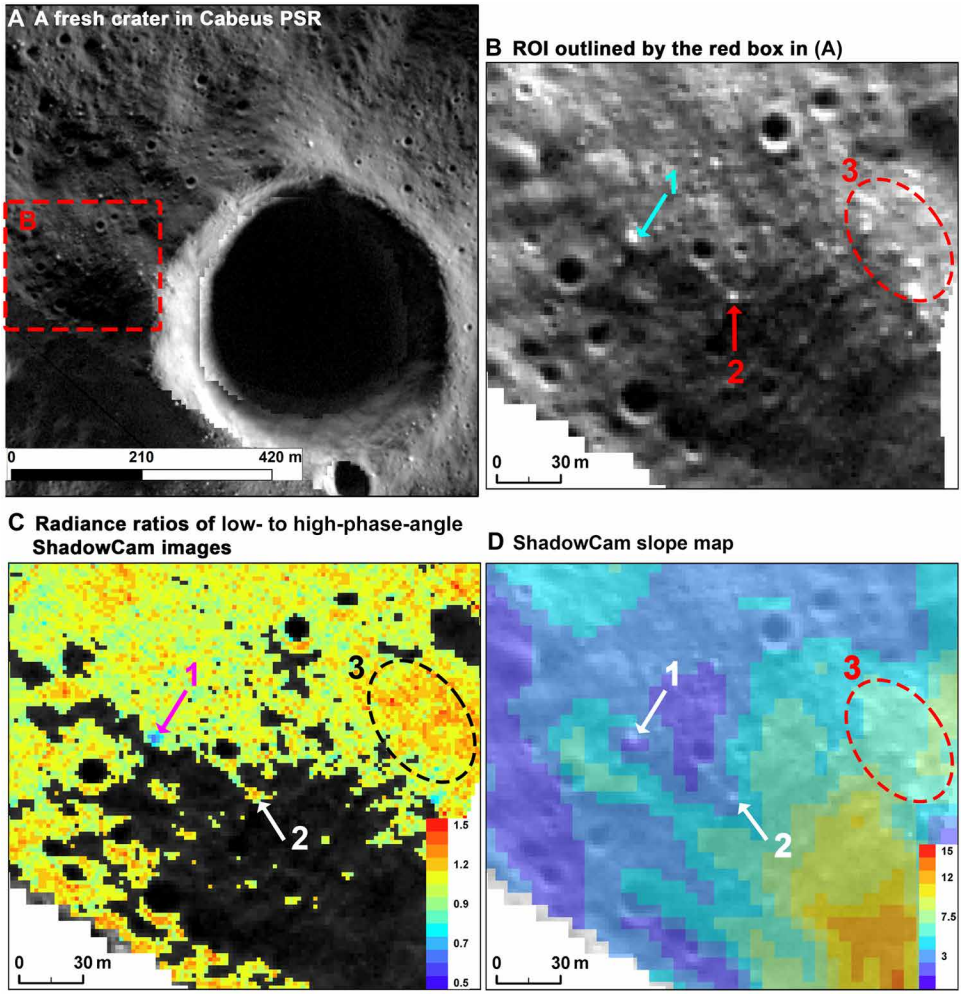

Fig. 6. Forward-scattering anomaly seen nearby a fresh crater in the Cabeus PSR. (**A**) ShadowCam image (M042280830SE) at a fresh crater (380-m diameter) in the Cabeus PSR. (**B**) Zoomed-in view of the red box in (A). ROIs 1 and 2 are spots ~3× and ~2× brighter than the background, respectively. The oval outlines bright boulders (ROI 3). (**C**) Ratio map of ShadowCam stereo observations of the region in (B). Note that doubly shaded regions that have very low SNRs (low radiance) are masked. (**D**) The slope map derived from the ShadowCam stereo observations at the same region in (B). Note that the spatial resolution in (A) to (C) is around 1.8 m/pixel, while that in (D) is 6 m/pixel.

locations, including temporarily shadowed regions at low latitudes, we observed that boulders are brighter than the surrounding regolith (Figs. 2 and 3 and fig. S1). This suggests that the bright boulders seen in cold traps are not necessarily associated with ice. However, we cannot rule out the possibility that some boulders in PSRs may contain ice, because ice-bearing boulders would also display high reflectance in ShadowCam observations. A full coverage of lunar PSRs with ShadowCam observations at complementary phase angles (e.g., separated by >~20°) can help identify forward-scattering anomalies that might be indicative of water ice.

Determining the absolute phase angles of scattered light in PSRs remains a substantial challenge. However, because the two ShadowCam stereo images were acquired only around 2 hours apart, we can assume similar incidence angles for scattered light. Multiple light sources scattered into PSRs make it challenging to compute incidence angles and, thus, phase angles (*60*–*62*). We used a ray tracing model to estimate the scattered incidence, emittance, and phase angles under ShadowCam observation conditions (see Methods). The derived median incidence angles of the two ShadowCam images in paired stereo observations show <2° difference (fig. S8). However, the ray tracing modeling work is computationally consuming and was only performed at a low spatial resolution scale of 60 m/pixel (e.g., fig. S8). The viewing angles at the ShadowCam observation scale (1.8 m/pixel) may vary strongly because of the presence of boulders, which needs to be further examined in future studies.

The interpretation of high-reflectance anomalies such as those shown in Fig. 4 and fig. S2A may not be unique. Those bright spots are around 10 to 20 m in size. Across multiple observations with varying illumination conditions, the pixels corresponding to the bright spot in Fig. 4 consistently maintained radiance values about 50 to 60% higher than the immediate surroundings. Such reflectance contrast is commonly seen in boulders, fresh craters and ejecta, recent landslides, and their surroundings (Fig. 2). Although craters in the 10- to 20-m diameter range can be well resolved in ShadowCam images (e.g., fig. S3) and we can also rule out the possibilities of boulders, landslides, and bedrocks from the ShadowCam images under

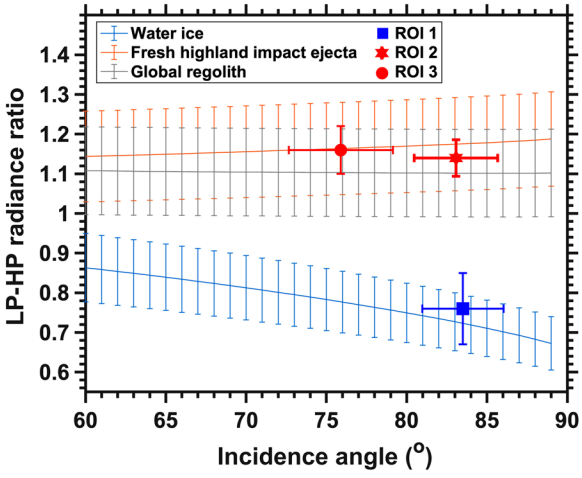

Fig. 7. Radiance ratios of ShadowCam stereo observations at LP and HP angles (LP/HP) at ROIs 1 to 3 compared with model results. Ratio values and standard deviations of ROIs 1 to 3 were from Fig. 6C. Median incidence angles and their standard deviations of ROIs 1 to 3 were modeled at 60 m/pixel (fig. S8). The LH/HP radiance ratios were modeled using Hapke's radiative transfer model with parameters derived from previous studies (see Methods). Error bars in the model results are 10% uncertainty sourced from the Hapke model (*57*).

multiple illumination conditions at those bright spots (Fig. 4 and fig. S3), it is unclear whether they are outcrops or deposits of high-reflectance materials such as immature anorthosite rather than water ice. We also observed abnormally bright wall materials at small craters in PSRs similar to those in fig. S6. Although these craters do not exhibit bright ejecta, indicating that they are not fresh impacts (fig. S6), the bright wall materials could be fresh exposures of regolith or bedrock exposed by recent mass wasting. Another possibility is the presence of water ice. Stereo observations at the Hermite A bright spot confirm that it is less backscattering than other high-reflectance regions nearby (fig. S2B), which is indicative of the presence of high-reflectance and forward-scattering materials similar to water ice. Future observations at varying phase angles of the de Gerlache bright spot (Fig. 4) and many other high-reflectance materials (fig. S6) can reveal the scattering properties and help to determine whether they show similar forward-scattering properties to water ice.

It is possible that factors such as regolith porosity and grain size also influence scattering behaviors. However, we have not seen reports suggesting that the porosity and grain size of lunar surface regolith can change its scattering properties markedly, such as from backscattering to forward scattering. In addition, the forward-scattering anomaly regions observed in Fig. 6 and figs. S2 and S7 are only slightly larger than the spatial resolution of the digital elevation models constructed from stereo images and used to georeference them [see Methods and (*63*)]. This proximity to the resolution limit introduces uncertainties in the ratios of stereo observations obtained for these areas. The small size (a few tens of meters) of these high-reflectance and forward-scattering anomalies also limits cross examinations from other datasets such as M^3 (280 m/pixel), LOLA albedo (500 m/pixel), and LAMP (240 m/pixel). Therefore, additional observations, particularly at varying phase angles, are necessary to determine whether these high-reflectance and forward-scattering anomaly regions are related to the presence of ice or result from other factors.

Our manual examination of ShadowCam radiance images that cover all lunar PSRs suggests either that most of the lunar PSRs lack surface ice exposures or that their ice concentration is below the detection limit, approximately 20 to 30 wt % on the basis of the visible reflectance enhancement (Fig. 1C), which aligns well with previous ShadowCam findings (*58*). Only a few candidate high-reflectance anomalies were seen (Fig. 4 and figs. S2A and S6), which, if they are water ice, is consistent with previous sparse detections of lunar surface water ice (*30*, *33*–*35*). We also examined six pairs of ShadowCam stereo images at Faustini, Slater, Cabeus, Wiechert J, Hermite A, and Mouchez L PSRs. Despite the small number of stereo images examined in this study, we found multiple spots (~20 to 50 m) showing high-reflectance and forward-scattering properties (e.g., the Hapke phase function parameter $c < 0$) (Fig. 6 and fig. S7), which is consistent with the optical properties of water ice, although other possibilities cannot be ruled out. We expect to see more similar exposures with both high reflectance and forward scattering to that in Fig. 6 in the future when more stereo images are acquired and calibrated during the KPLO extended mission. The higher number of exposures with high reflectance and forward scattering suggests the following: (i) Surficial water ice may be more widespread with low content rather than high content, considering that the detection limit based on scattering anomalies is lower than that assessed from high-reflectance anomalies (<10 wt % versus 20 to 30 wt %, Fig. 1, C and D); (ii) forward-scattering anomalies are commonly associated with boulders near fresh craters (Fig. 6 and fig. S7), which may suggest that buried water ice was excavated to the surface by impacts. This seems consistent with an independent study that systematically and statistically analyzed ShadowCam radiance variations at pixels with water ice detections from M^3 data as well as across PSRs with and without any M^3 ice detections (*64*). They found that radiance enhancements were observed exclusively when comparing "icy" PSRs (with M^3 ice detections) to "dry" ones (no M^3 ice detections) near the north pole, and such enhancements could not be explained by differences in illumination conditions, suggesting the wide presence of water ice (*64*). However, PSRs containing M^3 ice detections near the south pole did not exhibit such radiance enhancements compared to "dry" PSRs, aligning with the findings of sparse and low-abundance ice (*30*, *33*–*35*). Future missions that have a much lower detection limit of water ice ($\lesssim$1 wt %) than ShadowCam can help to verify and push further our findings and better map the distribution of surficial water ice in lunar PSRs.

METHODS

Estimation of impact-delivered water to the lunar and mercurian surface

The delivery of water to the surfaces of the Moon and Mercury through impacts is influenced by differences in impact flux, impactor size distribution, and impact velocities. Mercury experiences a significantly higher total flux of impactors smaller than 100 m, ~20 times greater than that on the Moon. This estimate was derived from the combination of a micrometeoroid flux (particles less than 100 μm) on Mercury, which is around 39 times higher than the Moon's, at 6.0×10^{-15} g cm^{-2} s^{-1} on Mercury versus 1.54×10^{-16} g cm^{-2} s^{-1} on the Moon (*65*), and a flux of larger meteoroids (1 cm to 100 m) that is around 10% of the Moon's, corresponding to ~4.9×10^{-19} g cm^{-2} s^{-1} on Mercury and ~4.9×10^{-18} g cm^{-2} s^{-1} on the Moon (*44*, *66*). Higher impact velocities on Mercury were suggested to result in

20 times more vaporization per impact than on the Moon (*37*). Although Mercury's greater flux and higher gravitational retention velocity could increase water delivery, its higher vaporization rates may cause proportionally greater water loss during impact. In contrast, the Moon may preserve a higher fraction of water from its impacts because of lower vaporization despite its lower overall flux and gravitational retention. Assuming similar water content in impactors, the net delivery of water to the surfaces of the Moon and Mercury may thus be comparable. Our estimates underscore the balance among impact flux, gravitational retention, and vaporization in governing water delivery to planetary surfaces, with potential refinements achievable through future studies incorporating retention efficiencies and secondary effects.

ShadowCam image preparation

ShadowCam onboard KPLO offers unprecedented imaging capabilities of lunar PSRs, providing small pixel scales (1.5 to 2.0 m) and high SNR (>100 for radiance >0.1 W m^{-2} sr^{-1} μm^{-1}) in the visible region (*50*, *53*). In our analysis, we used the calibrated radiance images (*53*). The exact illumination for each ShadowCam pixel is complex because of scattering of a broad range of light rays reflected from nearby topographic facets. The uncertainty in calculating the exact intensity of the scattered incoming light on individual pixels makes it difficult to derive accurate reflectance from ShadowCam images. However, the PSRs investigated here have relatively smooth crater floors. Therefore, we assumed that lighting conditions were uniform within each PSR, particularly at ROIs and their immediate surroundings. We then treated the acquired radiance data as a proxy for surface reflectance and compare pixels within individual PSRs, which allowed us to detect subtle variations that may indicate the presence of water ice.

We used ISIS3 software (*67*) modified by the ShadowCam team to prepare mosaics of ShadowCam images. We first searched all ShadowCam images in PSRs of interest using these criteria: emittance angles <1°, spatial resolutions better than 1.8 m/pixel, and subsolar latitudes >1.3° (north pole summer) or <−1.3° (south pole summer) depending on the pole. If there is more than one ShadowCam image in a given region, we will manually pick the one with the highest radiance (strongest signal) for mosaicking. We focused on all PSRs in both ~80° to 90° polar caps. The selected ShadowCam images were then mosaicked at their intrinsic spatial resolution. We then manually examined the mosaicked ShadowCam images using ArcGIS. The regions with M^3 ice detections (*34*) were mainly checked for signs of ice, but other regions in individual PSRs were also carefully examined at the pixel scale to search for high-reflectance anomalies.

ShadowCam stereo image preparation

More than one observation would be needed at the same region but from different phase angles to assess the possible presence of forward-scattering materials on the lunar surface. We used ShadowCam stereo pairs that are acquired at two different phase angles. ShadowCam has been obtaining stereo observations by slewing the spacecraft ~22° since late 2023 (fig. S5) (*63*). The stereo images were acquired with only a 2-hour time difference and, thus, almost identical lighting conditions and incidence angles (e.g., fig. S8) but with different emissions and, thus, phase angles (fig. S5), which could provide a first look at the change in reflectance as a function of phase angle. We assumed that the lighting conditions remained the same between two stereo observations and compared the radiance measurements directly. By taking the ratio of radiance values at different phase angles, we can assess how surface scattering varies spatially.

The ShadowCam team creates digital terrain models (DTMs) from specially targeted geometric stereo observations using US Geological Survey ISIS (Integrated Software for Imagers and Spectrometers) and SOCET SET from BAE Systems (*63*). The images are aligned by bundle-adjusting a set of "tie points" that are chosen by matching pixels between the images. Between 20 and 300 tie points are used for each stereo set, depending on the size of the PSR, the number of images used, and the complexity of the topography. SOCET SET reports the root mean square error (RMSE) of all the tie point residuals included in the bundle adjustment; this RMSE is considered acceptable when it is less than 0.5 pixels. The ShadowCam DTMs have RMSE errors <0.5 pixels, and all DTMs used in this study except for Hermite A had RMSE <0.28 pixels, indicating tight alignment between the images. The DTMs used in this work had tie point residuals <1 pixel, except for Hermite A, whose tie points had residuals <2.1 pixels.

The ShadowCam DTMs are created at a 3× native image resolution (3 to 7 m/pixel) and are controlled to the most accurate LOLA point data available at the time the DTM was created, with average offsets from LOLA of ≤5.2 m horizontally and ≤ 1.0 m in elevation. The ShadowCam team produces orthophotos by reprojecting the stereo images against the DTM, removing distortion resulting from camera obliquity to create map products at the images' native pixel scale. The RMSE values and tie point residuals, as well as qualitative examination, indicate that the orthophotos used in this work are aligned to the input DTM and to each other with offsets of less than 2 pixels. We manually examined the offsets of our studied regions at Hermite A (fig. S2), Faustini (fig. S7), and Cabeus (Fig. 6) and confirmed that their possible offsets are about a pixel or less.

We loaded the stereo images into ArcGIS and produced ratios of each pair of images. The relative change of phase angles in each stereo pair was computed on the basis of the positions of the sun, local topography highs where the sunlight was scattered into PSRs, and the spacecraft before and after slewing (figs. S5 and S8). We ratioed the ShadowCam image with the LP angle to the one with the HP angle (LP/HP) in each pair of stereo observations.

Illumination model to derive viewing angles of scattered light in PSRs

We performed complex illumination modeling calculations to understand the secondary lighting geometry in lunar PSRs. We used IllumNG software, which has scattering computation capabilities as described in (*68*). Photometric interactions at the surface of shadowed terrain are made complicated because there is no single lighting source like the Sun on sunlit terrain but rather an extended, nonuniform, ever-changing source landscape. Instead of a single set of incidence, emission, and phase angles, there is continuum, originating from all visible sunlit locations with their own radiance. We can attempt to use effective incidence, emission, and phase angles to be used in photometric analysis. Following (*54*) and (*69*), for each pixel, we compute the weighted median of these angles, with the importance of any sunlit pixel weighted by the radiance observed by ShadowCam that it contributes. Thus, we account for the photometric effects of both the first (sunlit) and second (shadowed) bounces to obtain the most representative angles. For our raytracing

computations, we use the updated topography models from (*70*), at a resolution of 60 m/pixel to balance the computational cost of scattering simulations. First, we determine the direct illumination from an extended Sun (accurately modeling partial solar visibility and the resulting soft shadows). Then, the double bounces from all elements of the mesh visible from all evaluated points are modeled photometrically, i.e., we do not limit the number of elements or rays to consider [Monte Carlo approaches are sometimes to speed up computations in large-scale simulations; e.g., (*19*)]. In this work, the evaluated pixels had typically 40,000 to 100,000 scattering elements.

Radiative transfer modeling of the ShadowCam radiance ratio

Reflectance under the scattered light condition in lunar PSRs may be more relevant to hemispherical-directional reflectance by definition. However, because of the fact that most PSRs are formed in craters and the scattered light is mostly from one side of the illuminated wall, which limits the spread of light sources, most scattered light could be only from a narrow-illuminated belt on the crater wall (*62*, *71*). So, even though the light scattered into those ShadowCam pixels is not collimated, the incidence angles of those scattered light are within in a narrow range with standard deviations mostly <3° (fig. S8, C and D). Thus, we assume that the light source is quasi-collimated and thus use the bidirectional reflectance equation of Hapke's model.

We used Hapke's radiative transfer model (*72*) and the parameters derived in previous remote observations to model the radiance ratios of ShadowCam stereo observations. In the Hapke model, reflectance R or I/F (I: radiance; F: irradiance) can be described as a function of single scattering albedo ω and effects from viewing geometry, back surging [$B(g, \varphi)$], phase function [$P(g)$], two-stream multiple scattering function (H), and macro surface roughness (S) (*72*, *73*).

$$R = \frac{I}{F} = \frac{\omega}{4}\frac{\mu_0}{\mu+\mu_0}\left\{\left[1+B(g)\right]P(g)+H(\mu_0,\omega)H(\mu,\omega)-1\right\}S(i,e,g,\bar{\theta}) \quad (1)$$

where μ_0 is the cosine of the incidence angle (i), μ is the cosine of the emergence angle (e), g is the phase angle, φ is the porosity, and $\bar{\theta}$ is the surface slope. We used a two-term Henyey-Greenstein (HG) polynomial as the phase function (*57*, *73*). We assume that I_1 and I_2 are the ShadowCam radiance acquired at the LP and HP angles in each pair of stereo observations, respectively. Given that the two images were acquired only around 2 Earth hours apart (the lunar day length is around 350 Earth hours), we can assume that the change of incident scattered light intensity (F_1 and F_2) in the same region is negligible and $F_1 = F_2$. The ratio of reflectance between LP and HP can then be modeled as

$$\frac{I_1/F_1}{I_2/F_2} = \frac{\frac{\omega}{4}\frac{\mu_0}{\mu_1+\mu_0}\left\{\left[1+B(g_1)\right]P(g_1)+H(\mu_0,\omega)H(\mu_1,\omega)-1\right\}S(i,e_1,g_1,\bar{\theta})}{\frac{\omega}{4}\frac{\mu_0}{\mu_2+\mu_0}\left\{\left[1+B(g_2)\right]P(g_2)+H(\mu_0,\omega)H(\mu_2,\omega)-1\right\}S(i,e_2,g_2,\bar{\theta})} \quad (2)$$

then we can get

$$I_1/I_2 = \frac{\mu_2+\mu_0}{\mu_1+\mu_0}\frac{\left\{\left[1+B(g_1)\right]P(g_1)+H(\mu_0,\omega)H(\mu_1,\omega)-1\right\}}{\left\{\left[1+B(g_2)\right]P(g_2)+H(\mu_0,\omega)H(\mu_2,\omega)-1\right\}}\frac{S(i,e_1,g_1,\bar{\theta})}{S(i,e_2,g_2,\bar{\theta})} \quad (3)$$

We can then model the radiance ratio to let the incidence angle vary from 0° to 90° and at two emittance angles of images in each pair of ShadowCam stereo observations. From our image selection, the two emittance angles are ~0° (nadir observations) and 20° (slewed observations). The phase angle g can be easily derived from the incidence, emittance, and azimuth angles of ShadowCam observations. We also need the parameter values for ω, $\bar{\theta}$, and coefficients (b and c) for the phase function. We used the values of ω, $\bar{\theta}$, b, and c for the lunar surface derived from the LROC WAC data (Table 1) (*49*). We used the water ice values of ω, $\bar{\theta}$, b, and c derived from the Martian polar ice cap (Table 1) (*48*). For the lunar surface material, we modeled two end-members, one of which is the global lunar regolith, while the other is fresh highland impact ejecta. The lunar polar region is suggested to be dominated by anorthosite, like the highlands. Fresh highland impact ejecta shows the strongest backscattering (*49*) and thus was chosen for modeling (Table 1).

Determining the detection limit of water ice

The detection limits of water ice that can be determined by using the reflectance enhancement and scattering properties were based on the performance of the ShadowCam instrument. To search for surficial water ice via reflectance enhancement, we assessed how much the reflectance of a region is elevated compared with its surroundings. Studies suggested that ShadowCam is able to resolve reflectance contrasts higher than around 20% in lunar PSRs (*54*). Although the exact phase angles of ShadowCam observations are unknown, modeling work suggests that most of the phase angles of ShadowCam observations are between 30° and 100° (*61*, *62*). We modeled how

Table 1. Parameters of our radiative transfer model. Parameter values and their sources used to model the radiance ratio of ShadowCam stereo images.

	Global regolith	Fresh highland ejecta	Pure water ice	References
ω	0.41	0.49	0.8	(*48*, *49*)
i	0°–90°	0°–90°	0°–90°	This work
e	0; 20	0; 20	0; 20	This work
g	0°–110°	0°–110°	0°–110°	This work
b	0.3	0.2	0.5	(*48*, *49*)
c	0.2	0.7	−0.6	(*48*, *49*)
φ	0.6	0.6	0.6	(*72*)
$\bar{\theta}$	23°	23°	23°	(*49*)

the reflectance of water ice and lunar regolith mixtures varies with the water ice content at phase angles of 30° and 100° (Fig. 1C). The intersections of the 20% reflectance enhancement with the two trend lines of reflectance enhancement at different ice contents defined the detection limits of water ice by ShadowCam, which are 30 and 20 wt % at 30° and 100° phase angles, respectively (Fig. 1C). Searching for water ice by assessing the scattering property, we ratio the ShadowCam radiance of the same region at different phase angles. Therefore, the detection limit of water ice would depend on the radiometric calibration of ShadowCam. The uncertainty of the radiometric calibration of the ShadowCam radiance data is around 5% (*53*). We modeled the reflectance enhancement of water ice and lunar regolith mixtures at different phase angles for four ice content cases of 1, 5, 10, and 20 wt %. Reflectance enhancements are notably stronger at HP angles, which is attributed to the forward scattering of water ice. We found that the reflectance enhancement is higher than 5% for mixtures with ice contents greater than 5 wt % at phase angles between 30° and 100° (Fig. 1D). It should be noted that the above reflectance enhancements were based on comparison with dry regolith. If the regolith in the studied regions contains water ice, the detection limits would be higher than 20 to 30 wt % and 5 wt % if examining the reflectance contrast and scattering properties, respectively.

We used the Hapke radiative transfer model (Eq. 1) to derive how the visible reflectance changes with phase angle when the lunar regolith is mixed with water ice. To model the reflectance of water ice and lunar regolith mixtures, we first calculated the average ω_{ave} of the binary mixtures (*73*)

$$\omega_{ave} = \frac{\frac{m_i\omega_i}{\rho_i D_i} + \frac{m_r\omega_r}{\rho_r D_r}}{\frac{m_i}{\rho_i D_i} + \frac{m_r}{\rho_r D_r}} \quad (4)$$

where m_i, ω_i, ρ_i, and D_i are the mass fraction, single scattering albedo, density, and grain size of water ice, respectively; m_r, ω_r, ρ_r, and D_r are the mass fraction, single scattering albedo, density, and grain size of lunar regolith, respectively. We tested the mass fractions of water ice at 1, 5, 10, and 20 wt %, and the respective mass fractions of lunar regolith are 99, 95, 90, and 80 wt %. The ω_i and ω_r were derived using Eq. 1 as well as the reflectance of water ice and the global average M^3 spectrum at 700 nm in Fig. 1. The densities of water ice and lunar regolith are set to 0.9 and 1.8 g/cm^3 (*74*), respectively. The grain size of water ice and lunar regolith is set to 15 μm because a previous study suggested that the 10- to 20-μm grain size group of lunar regolith dominated the visible reflectance feature of the bulk regolith (*75*).

We also computed the phase function of the binary mixtures. The average phase function can be calculated as (*73*)

$$P_{ave} = \frac{\frac{m_i\omega_i P_i}{\rho_i D_i} + \frac{m_r\omega_r P_r}{\rho_r D_r}}{\frac{m_i\omega_i}{\rho_i D_i} + \frac{m_r\omega_r}{\rho_r D_r}} \quad (5)$$

The two new parameters P_i and P_r in Eq. 5 compared with Eq. 4 are the phase function of water ice and lunar regolith, respectively. The *b* and *c* parameters for the HG phase function of water ice are set to 0.5 and −0.6, respectively, which are derived from the Martian ice cap (*48*). The *b* and *c* values of the HG phase function of lunar regolith are set to 0.3 and 0.2, respectively, which are derived from the LROC WAC data (*49*).

Supplementary Materials

This PDF file includes:

Figs. S1 to S8
Table S1

REFERENCES

1. H. C. Urey, *The Planets: Their Origin and Development* (Yale Univ. Press, 1952), pp. 245.
2. K. Watson, B. C. Murray, H. Brown, The behavior of volatiles on the lunar surface. *J. Geophys. Res.* **66**, 3033–3045 (1961).
3. J. R. Arnold, Ice in the lunar polar regions. *J. Geophys. Res. Solid Earth* **84**, 5659–5668 (1979).
4. J. A. Zhang, D. A. Paige, Cold-trapped organic compounds at the poles of the Moon and Mercury: Implications for origins. *Geophys. Res. Lett.* **36**, L16203 (2009).
5. M. A. Slade, B. J. Butler, D. O. Muhleman, Mercury radar imaging: Evidence for polar ice. *Science* **258**, 635–640 (1992).
6. J. K. Harmon, P. J. Perillat, M. A. Slade, High-resolution radar imaging of Mercury's north pole. *Icarus* **149**, 1–15 (2001).
7. D. J. Lawrence, W. C. Feldman, J. O. Goldsten, S. Maurice, P. N. Peplowski, B. J. Anderson, D. Bazell, R. L. McNutt Jr., L. R. Nittler, T. H. Prettyman, D. J. Rodgers, S. C. Solomon, S. Z. Weider, Evidence for water ice near Mercury's north pole from MESSENGER Neutron Spectrometer measurements. *Science* **339**, 292–296 (2013).
8. G. A. Neumann, J. F. Cavanaugh, X. Sun, E. M. Mazarico, D. E. Smith, M. T. Zuber, D. Mao, D. A. Paige, S. C. Solomon, C. M. Ernst, O. S. Barnouin, Bright and dark polar deposits on Mercury: Evidence for surface volatiles. *Science* **339**, 296–300 (2013).
9. N. L. Chabot, C. M. Ernst, B. W. Denevi, H. Nair, A. N. Deutsch, D. T. Blewett, S. L. Murchie, G. A. Neumann, E. Mazarico, D. A. Paige, J. K. Harmon, J. W. Head, S. C. Solomon, Images of surface volatiles in Mercury's polar craters acquired by the MESSENGER spacecraft. *Geology* **42**, 1051–1054 (2014).
10. A. N. Deutsch, G. A. Neumann, J. W. Head, New evidence for surface water ice in small-scale cold traps and in three large craters at the north polar region of Mercury from the Mercury Laser Altimeter. *Geophys. Res. Lett.* **44**, 9233–9241 (2017).
11. V. R. Eke, D. J. Lawrence, L. F. Teodoro, How thick are Mercury's polar water ice deposits? *Icarus* **284**, 407–415 (2017).
12. T. Platz, A. Nathues, N. Schorghofer, F. Preusker, E. Mazarico, S. E. Schröder, S. Byrne, T. Kneissl, N. Schmedemann, J.-P. Combe, M. Schäfer, G. S. Thangjam, M. Hoffmann, P. Gutierrez-Marques, M. E. Landis, W. Dietrich, J. Ripken, K.-D. Matz, C. T. Russell, Surface water-ice deposits in the northern shadowed regions of Ceres. *Nat. Astron.* **1**, 0007 (2016).
13. T. Prettyman, N. Yamashita, M. J. Toplis, H. McSween, N. Schörghofer, S. Marchi, W. C. Feldman, J. Castillo-Rogez, O. Forni, D. J. Lawrence, E. Ammannito, B. L. Ehlmann, H. G. Sizemore, S. P. Joy, C. A. Polanskey, M. D. Rayman, C. A. Raymond, C. T. Russell, Extensive water ice within Ceres' aqueously altered regolith: Evidence from nuclear spectroscopy. *Science* **355**, 55–59 (2017).
14. S. Schröder, N. Schörghofer, E. Mazarico, U. Carsenty, Spectral properties of bright deposits in permanently shadowed craters on Ceres. *Astron. Astrophys.* **688**, A178 (2024).
15. N. Schorghofer, E. Mazarico, T. Platz, F. Preusker, S. E. Schröder, C. A. Raymond, C. T. Russell, The permanently shadowed regions of dwarf planet Ceres. *Geophys. Res. Lett.* **43**, 6783–6789 (2016).
16. N. Schorghofer, R. Gaskell, E. Mazarico, J. Weirich, History of Ceres's cold traps based on refined shape models. *Planet. Sci. J.* **5**, 99 (2024).
17. N. Schörghofer, R. Rufu, Past extent of lunar permanently shadowed areas. *Sci. Adv.* **9**, eadh4302 (2023).
18. M. Siegler, D. Paige, J.-P. Williams, B. Bills, Evolution of lunar polar ice stability. *Icarus* **255**, 78–87 (2015).
19. D. A. Paige, M. A. Siegler, J. A. Zhang, P. O. Hayne, E. J. Foote, K. A. Bennett, A. R. Vasavada, B. T. Greenhagen, J. T. Schofield, D. McCleese, M. C. Foote, E. DeJong, B. G. Bills, W. Hartford, B. C. Murray, C. C. Allen, K. Snook, L. A. Soderblom, S. Calcutt, F. W. Taylor, N. E. Bowles, J. L. Bandfield, R. Elphic, R. Ghent, T. D. Glotch, M. B. Wyatt, P. G. Lucey, Diviner lunar radiometer observations of cold traps in the Moon's South Polar region. *Science* **330**, 479–482 (2010).
20. R. A. Simpson, G. L. Tyler, Reanalysis of Clementine bistatic radar data from the lunar south pole. *J. Geophys. Res. Planets* **104**, 3845–3862 (1999).
21. W. C. Feldman, S. Maurice, D. J. Lawrence, R. C. Little, S. L. Lawson, O. Gasnault, R. C. Wiens, B. L. Barraclough, R. C. Elphic, T. H. Prettyman, J. T. Steinberg, A. B. Binder, Evidence for water ice near the lunar poles. *J. Geophys. Res. Planets* **106**, 23231–23251 (2001).
22. D. B. Campbell, B. A. Campbell, L. M. Carter, J. L. Margot, N. J. S. Stacy, No evidence for thick deposits of ice at the lunar south pole. *Nature* **443**, 835–837 (2006).
23. A. Sanin, I. G. Mitrofanov, M. L. Litvak, B. N. Bakhtin, J. G. Bodnarik, W. V. Boynton, G. Chin, L. G. Evans, K. Harshman, F. Fedosov, D. V. Golovin, A. S. Kozyrev, T. A. Livengood, A. V. Malakhov, T. P. M. Clanahan, M. I. Mokrousov, R. D. Starr, R. Z. Sagdeev, V. I. Tret'yakov, A. A. Vostrukhin, Hydrogen distribution in the lunar polar regions. *Icarus* **283**, 20–30 (2017).

24. P. D. Spudis, D. B. J. Bussey, S. M. Baloga, J. T. S. Cahill, L. S. Glaze, G. W. Patterson, R. K. Raney, T. W. Thompson, B. J. Thomson, E. A. Ustinov, Evidence for water ice on the moon: Results for anomalous polar craters from the LRO Mini-RF imaging radar. *J. Geophys. Res. Planets* **118**, 2016–2029 (2013).
25. J. Mitchell, S. Lawrence, M. Robinson, E. Speyerer, B. Denevi, Using complementary remote sensing techniques to assess the presence of volatiles at the lunar north pole. *Planet. Space Sci.* **162**, 133–147 (2017).
26. T. McClanahan, A. M. Parsons, T. A. Livengood, J. J. Su, G. Chin, D. Hamara, K. Harshman, R. D. Starr, Evidence for widespread hydrogen sequestration within the Moon's South Pole cold traps. *Planet. Sci. J.* **5**, 217 (2024).
27. A. K. Boyd, B. W. Denevi, M. R. Henriksen, M. R. Manheim, M. S. Robinson, E. J. Speyerer, R. V. Wagner, Resource potential of lunar permanently shadowed regions. *Icarus* **377**, 114874 (2022).
28. A. Colaprete, P. Schultz, J. Heldmann, D. Wooden, M. Shirley, K. Ennico, B. Hermalyn, W. Marshall, A. Ricco, R. C. Elphic, D. Goldstein, D. Summy, G. D. Bart, E. Asphaug, D. Korycansky, D. Landis, L. Sollitt, Detection of water in the LCROSS ejecta plume. *Science* **330**, 463–468 (2010).
29. M. T. Zuber, J. W. Head, D. E. Smith, G. A. Neumann, E. Mazarico, M. H. Torrence, O. Aharonson, A. R. Tye, C. I. Fassett, M. A. Rosenburg, H. J. Melosh, Constraints on the volatile distribution within Shackleton crater at the lunar south pole. *Nature* **486**, 378–381 (2012).
30. E. A. Fisher, P. G. Lucey, M. Lemelin, B. T. Greenhagen, M. A. Siegler, E. Mazarico, O. Aharonson, J. P. Williams, P. O. Hayne, G. A. Neumann, D. A. Paige, D. E. Smith, M. T. Zuber, Evidence for surface water ice in the Lunar Polar regions using reflectance measurements from the Lunar Orbiter Laser Altimeter and temperature measurements from the Diviner Lunar radiometer experiment. *Icarus* **292**, 74–85 (2017).
31. R. Sridharan, S. M. Ahmed, T. P. Das, P. Sreelatha, P. Pradeepkumar, N. Naik, G. Supriya, The sunlit lunar atmosphere: A comprehensive study by CHACE on the Moon Impact Probe of Chandrayaan-1. *Planet. Space Sci.* **58**, 1567–1577 (2010).
32. M. Ohtake, Y. Nakauchi, S. Tanaka, M. Yamamoto, K. Onodera, H. Nagaoka, R. Nishitani, Plumes of water ice/gas mixtures observed in the Lunar Polar region. *Astrophys. J.* **963**, 124 (2024).
33. P. O. Hayne, A. Hendrix, E. Sefton-Nash, M. A. Siegler, P. G. Lucey, K. D. Retherford, J.-P. Williams, B. T. Greenhagen, D. A. Paige, Evidence for exposed water ice in the Moon's south polar regions from Lunar Reconnaissance Orbiter ultraviolet albedo and temperature measurements. *Icarus* **255**, 58–69 (2015).
34. S. Li, P. G. Lucey, R. E. Milliken, P. O. Hayne, E. Fisher, J. P. Williams, D. M. Hurley, R. C. Elphic, Direct evidence of surface exposed water ice in the lunar polar regions. *Proc. Natl. Acad. Sci. U.S.A.* **115**, 8907–8912 (2018).
35. L. Magaña, K. D. Retherford, B. D. Byron, A. R. Hendrix, C. Grava, K. E. Mandt, U. Raut, E. Czajka, P. O. Hayne, D. M. Hurley, G. R. Gladstone, M. J. Poston, T. K. Greathouse, W. Pryor, J. T. Cahill, A. Stickle, LRO-LAMP survey of Lunar South Pole Cold Traps: Implication for the presence of condensed H2O. *J. Geophys. Res. Planets* **127**, e2022JE007301 (2022).
36. P. Borin, G. Cremonese, F. Marzari, A. Lucchetti, Asteroidal and cometary dust flux in the inner solar system. *Astron. Astrophys.* **605**, 12 (2017).
37. M. J. Cintala, Impact-induced thermal effects in the lunar and Mercurian regoliths. *J. Geophys. Res. Planets* **97**, 947–973 (1992).
38. B. Jones, M. Sarantos, T. Orlando, A new in situ quasi-continuous solar-wind source of molecular water on Mercury. *Astrophys. J. Lett.* **891**, L43 (2020).
39. B. M. Jones, A. Aleksandrov, K. Hibbitts, M. Dyar, T. M. Orlando, Solar wind-induced water cycle on the Moon. *Geophys. Res. Lett.* **45**, 10959–10967 (2018).
40. B. J. Butler, The migration of volatiles on the surfaces of Mercury and the Moon. *J. Geophys. Res. Planets* **102**, 19283–19291 (1997).
41. A. Raponi, M. C. de Sanctis, A. Frigeri, E. Ammannito, M. Ciarniello, M. Formisano, J. P. Combe, G. Magni, F. Tosi, F. G. Carrozzo, S. Fonte, M. Giardino, S. P. Joy, C. A. Polanskey, M. D. Rayman, F. Capaccioni, M. T. Capria, A. Longobardo, E. Palomba, F. Zambon, C. A. Raymond, C. T. Russell, Variations in the amount of water ice on Ceres' surface suggest a seasonal water cycle. *Sci. Adv.* **4**, eaao3757 (2018).
42. W. Farrell, T. J. Stubbs, J. S. Halekas, R. M. Killen, G. T. Delory, M. R. Collier, R. R. Vondrak, Anticipated electrical environment within permanently shadowed lunar craters. *J. Geophys. Res. Planets* **115**, E03004 (2010).
43. M. Sarantos, R. M. Killen, D. Kim, Predicting the long-term solar wind ion-sputtering source at Mercury. *Planet. Space Sci.* **55**, 1584–1595 (2007).
44. E. S. Costello, R. R. Ghent, M. Hirabayashi, P. G. Lucey, Impact gardening as a constraint on the age, source, and evolution of ice on Mercury and the Moon. *J. Geophys. Res. Planets* **125**, e06172 (2020).
45. P. Pokorný, E. Mazarico, N. Schorghofer, Erosion of volatiles by micrometeoroid bombardment on Ceres and comparison to the Moon and Mercury. *Planet. Sci. J.* **2**, 85 (2021).
46. C. Tai Udovicic, K. R. Frizzell, G. R. L. Kodikara, M. Kopp, K. M. Luchsinger, A. Madera, M. L. Meier, T. G. Paladino, R. V. Patterson, F. B. Wroblewski, D. A. Kring, Buried ice deposits in lunar polar cold traps were disrupted by ballistic sedimentation. *J. Geophys. Res. Planets* **128**, e2022JE007567 (2023).
47. N. Schorghofer, O. Aharonson, The lunar thermal ice pump. *Astrophys. J.* **788**, 169–175 (2014).
48. A. C. Pascuzzo, T. Condus, S. Li, J. F. Mustard, Sensitivity analysis of ice/dust aerosol and phase function assumptions on Hapke spectral unmixing and band depth parameters of Martian water ice. *Icarus* **374**, 114804 (2022).
49. H. Sato, M. Robinson, B. Hapke, B. Denevi, A. Boyd, Resolved Hapke parameter maps of the Moon. *J. Geophys. Res. Planets* **119**, 1775–1805 (2014).
50. M. S. Robinson, S. M. Brylow, M. A. Caplinger, L. M. Carter, M. J. Clark, B. W. Denevi, N. M. Estes, D. C. Humm, P. Mahanti, D. A. Peckham, M. A. Ravine, J. A. Schaffner, E. J. Speyerer, R. V. Wagner, ShadowCam instrument and investigation overview. *J. Astron. Space Sci.* **40**, 149–171 (2023).
51. N. de Castro, S. Li, Laboratory experiments on the visible to near-infrared (VNIR) spectroscopy of water ice and lunar highland simulant mixtures: Effects of particle size, particle shape, phase angle, and ice abundance. *Icarus* **435**, 116578 (2025).
52. Z. Yoldi, A. Pommerol, B. Jost, O. Poch, J. Gouman, N. Thomas, VIS-NIR reflectance of water ice/regolith analogue mixtures and implications for the detectability of ice mixed within planetary regoliths. *Geophys. Res. Lett.* **42**, 6205–6212 (2015).
53. D. C. Humm, M. J. Kinczyk, S. M. Brylow, R. V. Wagner, E. J. Speyerer, N. M. Estes, P. Mahanti, A. K. Boyd, M. S. Robinson, Calibration of ShadowCam. *J. Astron. Space Sci.* **40**, 173–197 (2023).
54. E. Speyerer, M. Robinson, W. Carter, B. Denevi, A. Martin, "Interpreting the darkness: Equatorial ShadowCam images shed light on permanent shadows," in *55th Lunar and Planetary Science Conference* (Lunar and Planetary Institute, 2024).
55. P. G. Lucey, D. T. Blewett, G. J. Taylor, B. R. Hawke, Imaging of lunar surface maturity. *J. Geophys. Res. Planets* **105**, 20377–20386 (2000).
56. A. Boyd, M. Robinson, "LROC NAC global photometry: Terrain types and phase curves," in *50th Lunar and Planetary Science Conference* (Lunar and Planetary Institute, 2019).
57. B. Hapke, B. Denevi, H. Sato, S. Braden, M. Robinson, The wavelength dependence of the lunar phase curve as seen by the Lunar Reconnaissance Orbiter wide-angle camera. *J. Geophys. Res. Planets* **117**, E00H15 (2012).
58. M. Robinson, P. Mahanti, D. B. J. Bussey, L. M. Carter, B. W. Denevi, N. M. Estes, D. C. Humm, M. J. Kinczyk, S. Li, P. G. Lucey, E. Mazarico, M. A. Ravine, E. J. Speyerer, R. V. Wagner, J. P. Williams, "Seeing in the shadows," in *55th Lunar and Planetary Science Conference* (Lunar and Planetary Institute, 2024).
59. J. P. Williams, D. A. Paige, B. T. Greenhagen, E. Sefton-Nash, The global surface temperatures of the moon as measured by the diviner lunar radiometer experiment. *Icarus* **283**, 300–325 (2017).
60. P. Mahanti, T. J. Thompson, M. S. Robinson, D. C. Humm, View factor-based computation of secondary illumination within lunar permanently shadowed regions. *IEEE Geosci. Remote Sens. Lett.* **19**, 8027004 (2022).
61. E. Speyerer, A. Boyd, P. Mahanti, M. Robinson, B. Denevi, "Illuminating the darkness: Photometric analysis under diffuse lighting," in *55th Annual Meeting of the Division for Planetary Sciences* (American Astronomical Society, 2023), vol. 55, p. 8.
62. E. Mazarico, S. Bertone, P. Mahanti, E. J. Speyerer, R. V. Wagner, B. W. Denevi, S. Li, M. S. Robinson, "Scattered illumination modeling for ShadowCam," in *55th Lunar and Planetary Science Conference* (Lunar and Planetary Institute, 2024).
63. M. Manheim, M. Henriksen, R. Wagner, C. Michaud, S. Team, "ShadowCam digital terrain models of permanently shadowed regions," in *55th Lunar and Planetary Science Conference* (Lunar and Planetary Institute, 2024).
64. J. Ando, S. Li, M. Robinson, R. Wagner, Reflectance contrasts at possible lunar water ice exposures seen by ShadowCam. *Planet. Sci. J.* **6**, 62 (2024).
65. M. B. Syal, P. H. Schultz, M. A. Riner, Darkening of Mercury's surface by cometary carbon. *Nat. Geosci.* **8**, 352–356 (2015).
66. S. Marchi, A. Morbidelli, G. Cremonese, Flux of meteoroid impacts on Mercury. *Astron. Astrophys.* **431**, 1123–1127 (2005).
67. K. Becker, J. Anderson, L. Weller, T. Becker, "ISIS support for NASA mission instrument ground data processing systems," in *44th Lunar and Planetary Science Conference* (Lunar and Planetary Institute, 2013), p. 2829.
68. E. Mazarico, M. K. Barker, J. B. Nicholas, Advanced illumination modeling for data analysis and calibration. Application to the Moon. *Adv. Space Res.* **62**, 3214–3228 (2018).
69. A. Martin, B. Denevi, E. Speyerer, A. Boyd, H. Brown, Imaging in shadows: A comparison of craters observed in primary and secondary illumination with the Lunar Reconnaissance Orbiter Camera. *Planet. Sci. J.* **5**, 207 (2024).
70. M. K. Barker, E. Mazarico, G. A. Neumann, D. E. Smith, M. T. Zuber, J. W. Head, X. Sun, A new view of the lunar south pole from the Lunar Orbiter Laser Altimeter (LOLA). *Planet. Sci. J.* **4**, 183 (2023).
71. P. Mahanti, M. S. Robinson, D. C. Humm, R. V. Wagner, N. M. Estes, J.-P. Williams, Preliminary characterization of secondary illumination at Shackleton crater permanently shadowed region from ShadowCam observations and modeling. *J. Astron. Space Sci.* **40**, 131–148 (2023).

72. B. Hapke, Bidirectional reflectance spectroscopy: 1. Theory. *J. Geophys. Res. Solid Earth* **86**, 3039–3054 (1981).
73. B. Hapke, *Theory of Reflectance and Emittance Spectroscopy* (Cambridge Univ. Press, 2012); 10.1017/CBO9781139025683.
74. J. K. Mitchell, R. F. Scott, W. N. Houston, N. C. Costes, W. D. Carrier, L. G. Bromwell, "Mechanical properties of lunar soil: Density, porosity, cohesion and angle of internal friction," in *3rd Lunar and Planetary Science Conference* (Lunar and Planetary Institute, 1972), vol. 3, pp. 3235–3253.
75. C. Pieters, E. Fischer, O. Rode, A. Basu, Optical effects of space weathering: The role of the finest fraction. *J. Geophys. Res. Planets* **98**, 20817–20824 (1993).
76. S. G. Warren, R. E. Brandt, Optical constants of ice from the ultraviolet to the microwave: A revised compilation. *J. Geophys. Res. Atmos.* **113**, D14220 (2008).

Acknowledgments: We express our gratitude to the reviewers for insightful and fruitful comments and discussion that have significantly improved the quality of this work. We thank the ShadowCam team for outstanding efforts in mission operations and in preparing the high-quality datasets that made this work possible. **Funding:** S.L. acknowledges the support for this research by the National Aeronautics and Space Administration (NASA) KPLO Participating Scientist Program (80NSSC21K0710 and 80NSSC24K1728 awarded to S.L.). M.S.R., B.W.D., M.R.M., E.M., R.V.W., E.J.S., and P.M. were funded under the ShadowCam investigation (NASA's contract NNH17CG00C). **Author contributions:** Writing—original draft: S.L. Conceptualization: S.L., M.S.R., and B.W.D. Investigation: S.L., M.S.R., B.W.D., M.R.M., R.V.W., E.M., E.J.S., and P.M. Data curation and software: S.L., M.R.M., R.V.W., and E.M. Methodology: S.L. and E.M. Visualization: S.L. and B.W.D. Validation: S.L., M.R.M., and E.M. Writing—review and editing: S.L., M.S.R., B.W.D., E.M., and R.V.W. **Competing interests:** The authors declare that they have no competing interests. **Data, code, and materials availability:** All data and code needed to evaluate and reproduce the results in the paper are present in the paper and/or the Supplementary Materials. Calibrated, map-projected ShadowCam data used in this work can be downloaded from NASA's PDS at https://pds.shadowcam.im-ldi.com/. Calibrated, map-projected LROC NAC data used in this study can be found at NASA's PDS https://pds.lroc.im-ldi.com/data/. Custom scripts used for radiative transfer modeling are available at Zenodo: https://doi.org/10.5281/zenodo.18625702. This study did not generate new materials.

Submitted 3 October 2025
Accepted 19 February 2026
Published 18 March 2026
10.1126/sciadv.aec8211

ScienceAdvances

Searching for surficial water ice in lunar permanently shaded regions (PSRs) with ShadowCam

Shuai Li, Mark S. Robinson, Brett W. Denevi, Madeleine R. Manheim, Erwan Mazarico, Robert V. Wagner, Emerson J. Speyerer, and Prasun Mahanti

Sci. Adv. **12** (12), eaec8211. DOI: 10.1126/sciadv.aec8211

Science Advances (ISSN 2375-2548) is published by the American Association for the Advancement of Science. 1200 New York Avenue NW, Washington, DC 20005. The title *Science Advances* is a registered trademark of AAAS.